




# Polarimetric Observable-based Analysis of Spontaneous Emission in Heterogeneous Layered Scattering Environments

Haojie Ding, Xiaopeng Gao , Xueqiang Fan , Zhongyi Guo \*

School of Computer and Information, Hefei University of Technology, Hefei 230009, China

## ARTICLE INFO

### Keywords:

Spontaneous emission  
Polarization characteristics  
Monte Carlo simulation  
Light scattering  
Bidirectional reflectance distribution function

## ABSTRACT

Spontaneous emission plays a fundamental role in a variety of optical detection and imaging systems. However, due to the intrinsic complexity of its modeling and the additional challenges posed by heterogeneous layered scattering environments along the light propagation direction, accurately characterizing its behavior remains a significant challenge. To address this issue, this paper proposes a novel approach to calculate and analyze the polarimetric characteristics of spontaneous emission in complex scattering media. The approach integrates a bidirectional reflectance distribution function (BRDF) model to determine the initial polarization state of emission, followed by Monte Carlo photon-tracking simulations to model propagation and scattering processes. Physically interpretable polarimetric observables are employed to extract polarization signatures for effective target differentiation. Simulated results show that the method precisely captures polarization variations induced by structural heterogeneity. Notably, the optimal target discrimination performance of most polarimetric observables is achieved at a detection angle of approximately  $70^\circ$ . This study not only provides essential theoretical basis for the theoretical advancements and technological innovations in the field of polarimetric imaging and optical sensing, but also offers a practical and feasible method for achieving target detection and recognition in complex scattering media environments by harnessing the polarization characteristics of spontaneous emission.

## 1. Introduction

In the field of remote sensing, the infrared spontaneous emission of targets serves as a fundamental basis for target discrimination, recognition, and imaging, as it carries critical information such as material properties and temperature distribution [1]. Differences in radiation intensity and spectral characteristics [1] of various targets in the infrared band can be directly utilized to construct target feature databases. Moreover, selective control of spontaneous infrared emission has become increasingly important for applications such as infrared camouflage and thermal regulation, further underscoring the significance of understanding and exploiting thermal emission characteristics in imaging systems [2–4]. While thermal infrared imaging provides a valuable means for continuous observation [5], the effectiveness of conventional intensity-based detection methods is often compromised. As infrared spontaneous emission signals propagate through the atmosphere, scattering and absorption effects induced by inhomogeneous media [6], such as aerosols [7] and clouds [8], lead to signal attenuation and spectral distortion, making it particularly challenging to distinguish

camouflaged targets from complex backgrounds.

To overcome these limitations, polarization, as an intrinsic physical property of light, provides a new approach due to its high sensitivity to microstructural features of media and surface characteristics of targets [9,10]. Unlike intensity signals that merely reflect energy distribution, the state of polarization (SoP) [11] contains additional information such as the orientation of the optical vector and the degree of polarization (DoP) [12–14], which offers significant advantages in applications such as target recognition and media property retrieval [15–17]. For instance, in imaging through turbid media [6,18–20], intensity signals are easily distorted by scattering-induced attenuation, whereas polarization information, represented by various polarimetric observables [21,22], can effectively mitigate the impact of scattering distortion and thereby enhance imaging resolution. In remote sensing [23], polarization characteristics enable the discrimination of targets with different material properties, overcoming the limitations of traditional intensity-based imaging in distinguishing camouflaged targets from complex backgrounds. These characteristics of polarization make it a promising approach to addressing the inherent limitations of

\* Corresponding author.

E-mail address: [guozhongyi@hfut.edu.cn](mailto:guozhongyi@hfut.edu.cn) (Z. Guo).

<https://doi.org/10.1016/j.optlaseng.2025.109342>

Received 28 July 2025; Received in revised form 23 August 2025; Accepted 6 September 2025

Available online 11 September 2025

0143-8166/© 2025 Elsevier Ltd. All rights are reserved, including those for text and data mining, AI training, and similar technologies.

conventional optical technologies [24–27].

Building upon these complementary advantages, the integration of polarization characteristics with infrared spontaneous emission offers a promising pathway to further enhance target detection and imaging performance [28–30]. Infrared light combined with polarization detection can provide high-dimensional information that is highly sensitive to surface and structural details [31,32]. The combination of these two mechanisms enables the development of advanced remote sensing systems capable of operating effectively under complex atmospheric conditions. Nevertheless, realizing this technological integration presents two major challenges. On the one hand, modeling the infrared spontaneous emission of targets is inherently complex and computationally demanding. On the other hand, as radiative photons emitted by targets propagate through inhomogeneous media such as atmospheric aerosols and clouds, the random evolution of their polarization states is coupled with depolarization effects, significantly amplifying the impact of scattering interference on target recognition and imaging quality, and thus posing substantial challenges for the development of reliable remote sensing systems under such complex conditions [33,34].

To address these challenges, this study proposes a novel remote sensing system that integrates an infrared spontaneous emission model, which combines a geometric-based surface representation method known as the microfacet circle approach with the bidirectional reflectance distribution function (BRDF) [35–37], together with a layered polarimetric radiative transfer model. In the first stage, the proposed infrared spontaneous emission model is employed to investigate the polarization characteristics of self-emitted photons from the target surface. In the second stage, the propagation behavior of these photons through an inhomogeneous atmospheric environment is analyzed using the layered polarimetric radiative transfer model. Finally, the polarization information carried by the photons received by the detector is utilized to derive various polarimetric observables, which quantitatively reveal polarization characteristics from multiple perspectives, thereby

polarization  $\mathbf{S}_{\text{out}}$  can be described as:

$$\mathbf{S}_{\text{out}} = \mathbf{M} \mathbf{S}_{\text{in}}, \quad (3)$$

where  $\mathbf{M}$  in Eq. (3) is the Mueller matrix (MM), which is a  $4 \times 4$  matrix encoding the target's polarimetric response. And  $\mathbf{M}$  can be described as:

$$\mathbf{M} = \begin{bmatrix} m_{11} & m_{12} & m_{13} & m_{14} \\ m_{21} & m_{22} & m_{23} & m_{24} \\ m_{31} & m_{32} & m_{33} & m_{34} \\ m_{41} & m_{42} & m_{43} & m_{44} \end{bmatrix}. \quad (4)$$

The MM not only modulates the incident SV but also provides rich information about the target's polarimetric properties. Various observables, such as overall polarizance ( $P_p$ ), degree of spherical purity ( $P_s$ ), and descriptors derived from the determinant ( $DET$ ) and trace ( $TRA$ ) of MM, can be directly computed to characterize the sample:

$$P_s = \frac{\|\mathbf{m}\|}{\sqrt{3}}, \quad (5)$$

$$DET = |\hat{\mathbf{M}}| \quad (6)$$

$$TRA = m_{11} + m_{22} + m_{33} + m_{44}, \quad (7)$$

here  $\hat{\mathbf{M}}$  is obtained by normalizing  $\mathbf{M}$  with respect to  $m_{11}$ ,  $DET$  is the determinant of the normalized MM, and  $\mathbf{m}$  is the  $3 \times 3$  sub-matrix obtained by removing the first row and first column of  $\hat{\mathbf{M}}$ .

Beyond these direct observables, MM contains more complex information such as retardance and depolarization, which require decomposition techniques for extraction. Among them, parallel decomposition interprets a depolarizer as an incoherent sum of up to four polarization-pure systems [38,39], whose weights correspond to the eigenvalues of the covariance matrix  $\mathbf{H}$ , derived from MM:

$$\mathbf{H} = \frac{1}{4} \begin{bmatrix} m_{11} + m_{12} + m_{21} + m_{22} & m_{13} + m_{23} + i(m_{14} + m_{24}) & m_{31} + m_{32} - i(m_{41} + m_{42}) & m_{33} + m_{44} + i(m_{34} - m_{43}) \\ m_{13} + m_{23} - i(m_{14} + m_{24}) & m_{11} - m_{12} + m_{21} - m_{22} & m_{33} - m_{44} - i(m_{34} + m_{43}) & m_{31} - m_{32} - i(m_{41} - m_{42}) \\ m_{31} + m_{32} + i(m_{41} + m_{42}) & m_{33} - m_{44} + i(m_{34} + m_{43}) & m_{11} + m_{12} - m_{21} - m_{22} & m_{13} - m_{23} + i(m_{14} - m_{24}) \\ m_{33} + m_{44} - i(m_{34} - m_{43}) & m_{31} - m_{32} + i(m_{41} - m_{42}) & m_{13} - m_{23} - i(m_{14} - m_{24}) & m_{11} - m_{12} - m_{21} + m_{22} \end{bmatrix}. \quad (8)$$

enhancing imaging quality. Through the integration of these three stages, a comprehensive remote sensing framework is established to effectively address target detection tasks in complex inhomogeneous scattering environments.

## 2. Theory and method

### 2.1. Polarization representation and Mueller matrix analysis

The State of Polarization (SoP) is typically represented by the Stokes vector (SV), a  $4 \times 1$  vector comprising the total intensity  $I$  and  $Q$ ,  $U$ , and  $V$  correspond respectively to the differences between the  $0^\circ$  and  $90^\circ$  polarization components, the  $45^\circ$  and  $135^\circ$  polarization components, and the right-circular and left-circular polarization components.

$$\mathbf{S} = [I, Q, U, V]^T. \quad (1)$$

From the SV, a polarimetric observable,  $DoP$ , representing the depolarization characteristics of light, can be derived.

$$DoP = \sqrt{Q^2 + U^2 + V^2} / I. \quad (2)$$

The SoP changes after incident light interacts with a target. The relationship between the incident polarization  $\mathbf{S}_{\text{in}}$  and the emergent

Based on these eigenvalues,  $P_1, P_2, P_3$  can be calculated to provide a comprehensive description of depolarization behavior:

$$P_1 = \frac{\lambda_0 - \lambda_1}{tr\mathbf{H}}, \quad (9)$$

$$P_2 = \frac{(\lambda_0 - \lambda_2) + (\lambda_1 - \lambda_2)}{tr\mathbf{H}}, \quad (10)$$

$$P_3 = \frac{(\lambda_0 - \lambda_3) + (\lambda_1 - \lambda_3) + (\lambda_2 - \lambda_3)}{tr\mathbf{H}}. \quad (11)$$

Here,  $\lambda_0, \lambda_1, \lambda_2$  and  $\lambda_3$  are the four eigenvalues of matrix  $\mathbf{H}$ . In particular, the depolarization index  $P_\Delta$ , derived from IPPs, serves as an effective metric of overall depolarization:

$$P_\Delta = \frac{1}{\sqrt{3}} \sqrt{2P_1^2 + \frac{2}{3}P_2^2 + \frac{1}{3}P_3^2}. \quad (12)$$

Compared to scalar depolarization indices alone, IPPs enable a more nuanced discrimination of depolarization mechanisms, and are thus widely adopted in polarization studies [38,40].

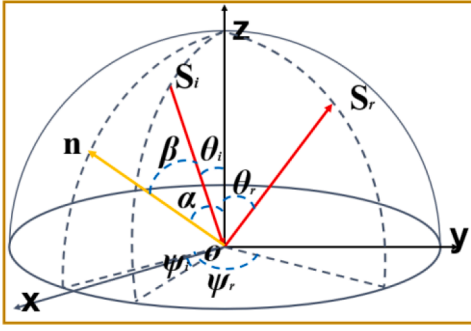


Fig. 1. Schematic of the BRDF.

## 2.2. BRDF modeling for rough surfaces with polarization

The bidirectional reflectance distribution function (BRDF) [41], originally formulated by Nicodemus in the 1970s, quantitatively relates the incident irradiance from a specific direction to the reflected radiance in another direction. Mathematically, it is defined as:

$$f_{BRDF}(\theta_i, \psi_i; \theta_r, \psi_r; \lambda) = \frac{dL_r(\theta_r, \psi_r)}{dE_i(\theta_i, \psi_i)} \quad (13)$$

where  $S_r$  and  $S_i$  represent the SV of the reflected radiance and the incident irradiance, respectively.

As shown in Fig. 1, the variables  $\theta$  and  $\psi$  denote the zenith and azimuth angles for both incidence (subscript  $i$ ) and reflection (subscript  $r$ ), and  $n$  represents the normal vector. Here,  $\alpha$  denotes the angle between the object surface normal and the microfacet normal, with the  $n$ -axis aligned along the microfacet normal direction.  $\beta$  represents the angle between the incident light direction and the microfacet normal. The relationships of  $\alpha$  and  $\beta$  with respect to the incidence and reflection angles  $(\theta_i, \theta_r, \psi_i, \psi_r)$  can be expressed as follows:

$$\cos\alpha = \frac{\cos\theta_i + \cos\theta_r}{2\cos\beta} \quad (14)$$

$$\cos(2\beta) = \cos\theta_i\cos\theta_r + \sin\theta_i\sin\theta_r\cos(\psi_r - \psi_i) \quad (15)$$

The BRDF is a deterministic function used to characterize the surface reflectance behavior. In particular, the microfacet theory models a rough surface as an ensemble of small, planar facets, each behaving as an ideal specular reflector governed by Fresnel laws. The distribution of these microfacets is typically assumed to follow a Gaussian function based on surface height statistics [35]:

$$D(\alpha) = \frac{1}{2\pi} \frac{e^{-\frac{\tan^2\alpha}{2\sigma^2}}}{\sigma^2 \cos^3\alpha} \quad (16)$$

The roughness of a target surface, as opposed to perfect smoothness, complicates scattered light interactions due to geometric occlusions referred to as the shadowing-masking effect. As surface roughness increases, this effect becomes more pronounced, significantly influencing the scattering behavior. Therefore, it is essential to incorporate shadowing considerations into the microfacet-based BRDF model to accurately represent rough surface characteristics. As for polarization light, the BRDF of a rough surface incorporating shadowing is mathematically expressed as:

$$f_{ij}(\theta_i, \psi_i; \theta_r, \psi_r; \lambda) = \frac{1}{8\pi} \frac{e^{-\frac{\tan^2\alpha}{2\sigma^2}}}{\sigma^2 \cos^4\alpha} \frac{1}{\cos\theta_r \cos\theta_i} G(\theta_i, \psi_i; \theta_r, \psi_r; \lambda) m_{ij}, \quad (17)$$

where  $G(\theta_i, \psi_i; \theta_r, \psi_r)$  [42] denotes the geometric attenuation factor caused by shadowing and masking and  $m_{ij}$  ( $i, j = 1, 2, 3, 4$ ) are the elements of the  $4 \times 4$  MM— $M(\theta_i, \psi_i; \theta_r, \psi_r)$ . Assuming that the material surface is isotropic and that  $\psi_i = 0$ , the shadowing function can then be

approximated as:

$$G(\theta_i, \theta_r, \psi_r) = \frac{1 + \frac{\omega_p |\tan\theta_p \tan\theta_r|}{1 + \sigma_r \tan\theta_p}}{[(1 + \omega_p \tan^2\theta_p)(1 + \omega_p \tan^2\theta_r)]} \quad (18)$$

where the calculation formulas for each variable are as follows:

$$\omega_p = \sigma_p \left( 1 + \frac{\pi}{\sin\alpha + v_p \cos\alpha} \right) \quad (19)$$

$$\tan\theta_{ip} = \tan\theta_i \frac{\sin\theta_i + \sin\theta_r \cos\psi_r}{2\sin\alpha \cos\beta} \quad (20)$$

$$\tan\theta_{rp} = \tan\theta_r \frac{\sin\theta_r + \sin\theta_i \cos\psi_i}{2\sin\alpha \cos\beta} \quad (21)$$

$$\tan\beta_p = \frac{|\cos\theta_i - \cos\beta|}{2\sin\alpha \cos\beta} \quad (22)$$

where,  $\sigma_p$ ,  $\sigma_r$ ,  $u_p$  and  $v_p$  are empirical parameters closely related to the surface roughness. Typically, these parameters are set to the following values:  $\sigma_p = 0.0136$ ,  $\sigma_r = 0.0136$ ,  $u_p = 9.0$ ,  $v_p = 1.0$  and  $\psi_i = 0$ .

The MM can be derived from Fresnel equations and the corresponding Jones matrix formulation [43].

In the present experiment, all materials involved are opaque, and thus, according to Kirchhoff's law of thermal radiation, emission is inherently related to reflection. Under the condition of thermal equilibrium, energy conservation dictates that the amount of energy absorbed by a target is equal to the amount it emits. Consequently, the emissivity of the target can be defined as:

$$\epsilon = \mathbf{E} - \begin{bmatrix} F_{11} & F_{12} & F_{13} & F_{14} \\ F_{21} & F_{22} & F_{23} & F_{24} \\ F_{31} & F_{32} & F_{33} & F_{34} \\ F_{41} & F_{42} & F_{43} & F_{44} \end{bmatrix}, \quad (23)$$

here,  $\mathbf{E}$  denotes the identity matrix, and the elements  $F_{ij}$  ( $i, j = 1, 2, 3, 4$ ) can be calculated using the following equation:

$$F_{ij} = \int \int_{\Omega} f_{ij}(\theta_i, \psi_i; \theta_r, \psi_r; \lambda) d\Omega. \quad (24)$$

Then, the SV:  $S_{sr}$ , corresponding to the spontaneous emission from the target, can then be computed using the following formula:

$$S_{sr} = \epsilon S_{in}, \quad (25)$$

## 2.3. Theory of photon scattering and propagation

Based on the ratio of the incident light's wavelength to the size of scattering particles, light scattering can generally be categorized into Rayleigh, Mie, and geometric regimes. Among them, Mie scattering is particularly applicable for modeling photon-particle interactions in media such as atmospheric or underwater environments. As discussed previously, the alteration of the SoP due to such interactions can be described using the MM. In the context of Mie scattering, the MM corresponding to single scattering events depends on the scattering angle  $\theta$  relative to the incident direction of light [44]. By employing the MM shown in Eq. (26), and the relation between incidence and output light shown in Eq. (3), the SoP of scattering light can be calculated. This angular dependence is expressed mathematically as:

$$M(\theta) = \begin{bmatrix} m_{11}(\theta) & m_{12}(\theta) & 0 & 0 \\ m_{21}(\theta) & m_{22}(\theta) & 0 & 0 \\ 0 & 0 & m_{33}(\theta) & m_{34}(\theta) \\ 0 & 0 & m_{43}(\theta) & m_{44}(\theta) \end{bmatrix}, \quad (26)$$

When polarized light propagates through a medium, its SoP is typically defined within a global coordinate system, usually aligned with the

Z-axis. However, during interactions with individual scattering particles, the SoP must be described relative to a local coordinate system associated with the particle. To accurately model the scattering process, it is therefore necessary to transform between the global and local coordinate systems [45]. In the case of a single scattering event, the process involves three stages: 1) rotating the SV from the global to the local coordinate system. 2) applying the scattering interaction in the local frame. 3) rotating the resulting SV back to the global coordinate system. This overall transformation can be described as:

$$\mathbf{M} = \mathbf{R}(\gamma_1)\mathbf{M}(\theta)\mathbf{R}(\gamma_2), \quad (27)$$

where  $\mathbf{R}$  is the rotation matrix. This transformation is achieved using rotation matrices, which modify the reference frame of the polarized light. The MM of a rotation operation has a standard form that depends on the rotation angle, and is mathematically equivalent to that of a linear retarder. The rotation matrix is given by:

$$\mathbf{R}(\gamma) = \begin{bmatrix} 1 & 0 & 0 & 0 \\ 0 & \cos(2\gamma) & \sin(2\gamma) & 0 \\ 0 & -\sin(2\gamma) & \cos(2\gamma) & 0 \\ 0 & 0 & 0 & 1 \end{bmatrix}, \quad (28)$$

In Eq. (27),  $\gamma_1$  and  $\gamma_2$  denote the pre-scattering and post-scattering rotation angles, respectively, and  $\theta$  is the scattering angle. These angles can be determined using the rejection sampling method [46]. For a single scattering event, the light is first transformed from the global coordinate system to the local coordinate system, interacts with a particle, and is then transformed back to the global system. This process is described by Eq. (27), where  $\theta$  and  $\gamma$  are derived via rejection sampling. In realistic scattering media, photons undergo multiple scattering

events, with each particle interaction modulating the SoP of the light. The final SoP after  $N$  scattering events is given by Eq. (29):

$$\mathbf{S}_{\text{out}} = \prod_{k=0}^N \mathbf{R}(\gamma_1)\mathbf{M}(\theta)\mathbf{R}(\gamma_2)\mathbf{S}_{\text{sr}}, \quad (29)$$

where  $\mathbf{S}_{\text{sr}}$  is the SV generated by the target's spontaneous emission.

#### 2.4. Scattering model and simulation procedure

This section details the scattering model and simulation procedure. Four distinct polarization states of incident light, represented by SV  $[1,0,0,0]^T$ ,  $[1,1,0,0]^T$ ,  $[1,0,1,0]^T$  and  $[1,0,0,1]^T$  respectively, with a wavelength of  $10 \mu\text{m}$ , are sequentially launched toward the target. For each polarization state,  $10^8$  photon samples are used to balance computational efficiency and accuracy. The target scene comprises three materials with distinct polarimetric characteristics: copper shaped as the letters “HFUT,” a circular opaque plastic region with a radius of 1 m, and a square stone region measuring  $2 \times 2$  m. The copper layer has a complex refractive index of  $1.1800 + 13.5600i$  and a surface roughness of 0.8; the opaque plastic layer is defined by  $1.6848 + 0.0210i$  with a roughness of 0.2; and the stone layer has a refractive index of  $1.6101 + 0i$  with a roughness of 0.8. These materials are deliberately selected to capture distinct refractive indices and surface roughness characteristics, thereby covering a broad range of typical polarization responses. While only three types of opaque objects are modeled, they are sufficient to reveal the general performance trends of the polarization observables in scattering environments.

During the interaction between light and target, a portion of the photons is absorbed and subsequently re-emitted into the scattering

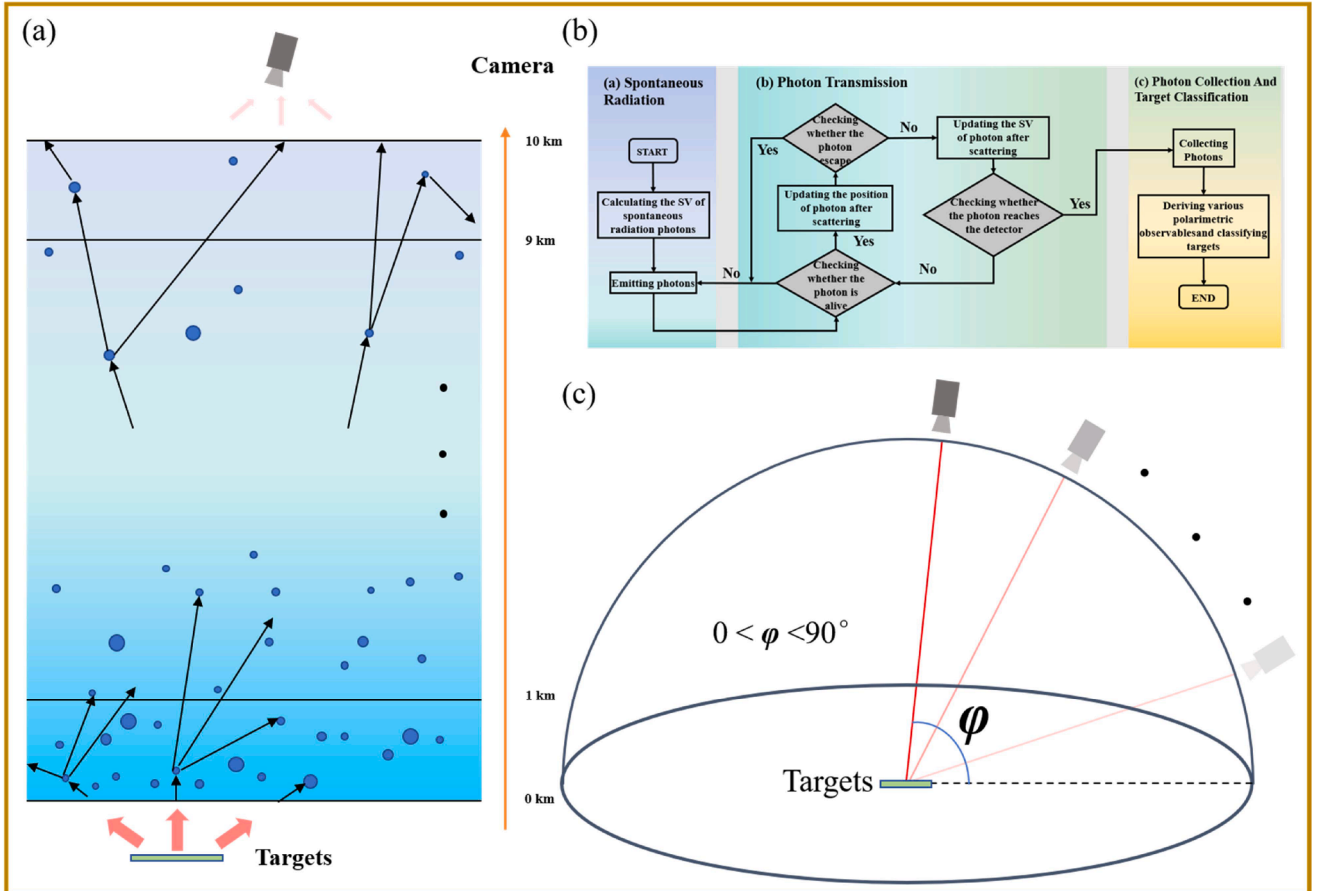


Fig. 2. (a) Picture of layered atmospheric scattering model. (b) Flow of the Monte Carlo simulation. (c) Schematic diagram of the relative position between the detector and the target in the model.

**Table 1**

The PND for 0–10 km measured in Hefei, Anhui, China.

	Clear sky	Overcast sky
Altitude(km)	PND(particle/cm <sup>3</sup> )	PND(particle/cm <sup>3</sup> )
0~1	2036.04	9730.02
1~2	890.55	3737.01
2~3	381.35	1259.05
3~4	173.40	461.15
4~5	104.54	167.54
5~6	76.62	76.62
6~7	61.18	61.18
7~8	58.84	58.84
8~9	59.44	59.44
9~10	57.47	57.47

medium as spontaneous emission. The SoP of these emitted photons is computed using the method described in Section 2.2.

As shown in Fig. 2(a), to simulate atmospheric inhomogeneity, the 10 km-thick scattering medium is divided into ten horizontal layers, each 1 km thick. As can be seen from Table 1, the physical parameters for each layer are configured based on real-world particle number distribution (PND) data measured in Hefei [47], covering the particle size ranges: 0.02–0.05  $\mu\text{m}$ , 0.05–0.1  $\mu\text{m}$ , 0.1–0.125  $\mu\text{m}$ , 0.125–0.25  $\mu\text{m}$ , 0.25–0.5  $\mu\text{m}$ , 0.5–0.8  $\mu\text{m}$ , 0.8–1.0  $\mu\text{m}$ , 1.0–1.25  $\mu\text{m}$ , 1.25–5  $\mu\text{m}$ , and 5–100  $\mu\text{m}$ . Specifically, in the simulation process, the extinction coefficient of the medium is used to determine the attenuation of photons before and after each scattering event. Since the extinction coefficient varies with altitude, the degree of attenuation also differs at each scattering step, and this effect accumulates continuously as scattering proceeds. To accurately capture this behavior, the attenuation is dynamically updated throughout the photon's propagation path. By employing the Monte Carlo method, these layer-dependent attenuation effects are naturally incorporated into the model, enabling a more realistic representation of the atmospheric environment and leading to more accurate results.

Photon propagation within the scattering medium is modeled as a sequence of single scattering events. The scattering direction after each interaction is determined using the rejection sampling method, while the scattering distance is initially calculated using the following equation:

$$l = -\frac{\ln \xi}{u_e}, \quad (30)$$

where  $\xi$  is a uniformly distributed random number between 0 and 1. This method works effectively in homogeneous media but becomes inadequate for layered structures, as it cannot accurately capture cross-layer transitions. Therefore, an improved approach based on transmittance is employed for stratified media. According to the Beer–Lambert law, the total transmittance is the product of transmittances across all layers, and the total distance  $l_s = l_1 + l_2 + l_3$  is derived from the logarithm of the combined transmittance. Based on the equation shown above, the total scattering distance can be written as:

$$l_s = l_1 + l_j + l_3 = l_1 + (j-1)l_2 + l_3, \quad (31)$$

where  $l_j = (j-1)l_2$  denotes the scattering distance sum of all the complete layers traversed along the scattering direction in a single scattering.

Consider a photon interacting with a particle at position  $P_0(x_0, y_0, z_0)$  propagating in the direction  $d_0(u_{x0}, u_{y0}, u_{z0})$ . The subsequent scattering distance is determined based on the azimuthal angle  $\phi$ , which leads to three distinct scenarios:

Case1:  $\cos(\phi) = 0$

In this case, the photon travels parallel to the current layer, so the next scattering event occurs within the same layer. The path length can be directly computed using Eq. (30).

Case2:  $\cos(\phi) > 0$

Here, the photon is forward-scattered. If it does not cross into the next layer, the remaining distance within the current layer is  $l_1 = (z_0 + j)/u_{z0}$ , while the distance to the next layer is  $l_2 = 1/u_{z0}$ . If  $l_{j+1} < l_1$ , scattering remains within the current layer; otherwise, the photon enters the subsequent layer. The distance  $l_3$  is determined according to Eq. (32), with the step function  $u(j-1)$  applied iteratively. The total scattering distance  $l_s$  is then obtained by combining  $l_1, l_2, l_3$  into Eq. (31).

$$l_3 = \frac{-\ln(\xi) - l_1 u_e^{-(i+1)} - \left( l_2 \sum_{k=1}^{j-1} u_e^{i+1-k} \right) u(j-1)}{u_e^{i-j+1}}, \quad (32)$$

Case3:  $\cos(\phi) < 0$

For backscattered photons, the initial distance is  $l_1 = (j + 1 - z_0)/u_{z0}$ . The calculation procedure follows the same framework as Case 2. In this scenario, all distances  $l_1, l_2, l_3$  are negative, reversing the judgment conditions. Near the ground, both forward and backward scattering are considered, accounting for the layer-dependent extinction coefficient  $u_e$  [48].

Once the scattering direction and distance are determined, the photon's new position is updated accordingly, and further scattering is evaluated recursively.

Based on the above-described photon scattering calculation method, the Monte Carlo algorithm is employed to track all photons throughout the entire simulation process. The detailed flow of the Monte Carlo simulation is illustrated in Fig. 2(b), which outlines key steps such as photon propagation, scattering direction and distance calculation, and polarization state updates. Within this simulation framework, the SoP of the scattered photons detected by the sensor can be obtained. Building upon this result, various polarimetric observables are then computed using the theoretical framework described in Section 2.1 to assess their imaging performance and target recognition capability. According to previous experimental studies [31], when the observation angle is smaller than 30° or approaches 90°, the DoP of spontaneous emission decreases significantly and strong depolarization occurs. Subsequent scattering processes further exacerbate this effect, making it difficult to obtain reliable results for other polarimetric observables. Therefore, to further investigate the impact of observation angle on imaging performance, simulations are conducted at six different viewing angles (30°, 40°, 50°, 60°, 70°, and 80°), enabling a comprehensive analysis of the angular response.

### 3. Results and analysis of the simulation

#### 3.1. The difference in imaging effect under different observation angles of incident light without any scattering medium

Different target regions exhibit distinct complex refractive indices and surface roughness, resulting in varying polarimetric characteristics of spontaneous emission, as described in Eq. (25). Consequently, the imaging performance across these regions is strongly influenced by the choice of polarimetric observable. Moreover, as indicated by Eq. (17), the observation angle is critical in determining how effectively different observables capture target-specific feature. To explore these dependencies, simulations are conducted across multiple observation angles.

As illustrated in Fig. 3, ten polarimetric observables are extracted through pixel-wise decomposition of the MM. The results reveal significant differences in the ability of these observables to characterize target features under various observation angles. At low observation angles, both the intensity  $I$  and the observable  $P_p$  exhibit poor performance in distinguishing between marble and plastic, failing to effectively reveal



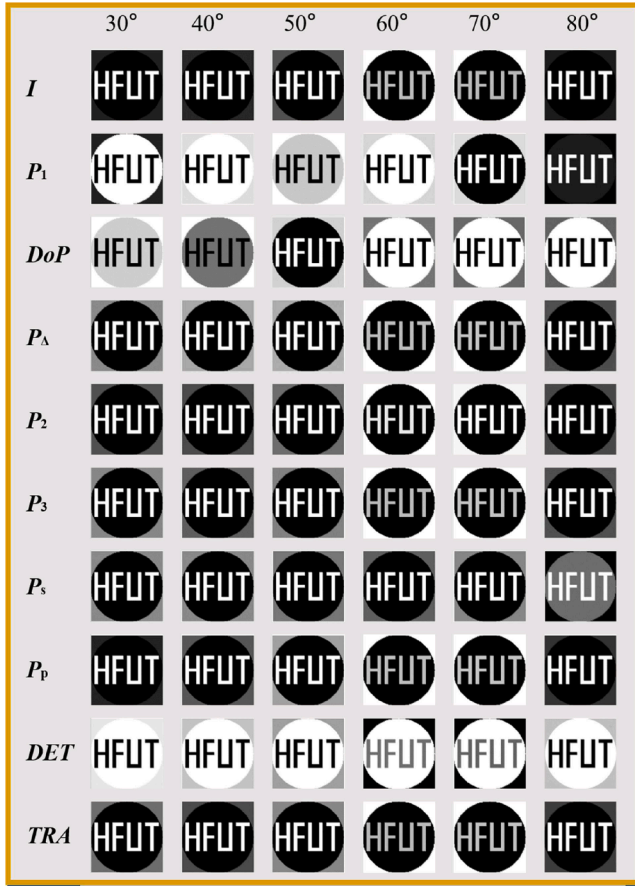


Fig. 3. The polarimetric observables at different angles in a non-scattering medium environment.

material boundaries or structural variations. Although the imaging performance of  $P_1$  fluctuates noticeably as the observation angle increases, it lacks a consistent and interpretable trend, which limits its practical value in complex scattering environments.

In contrast, the observable  $P_s$  maintains a relatively stable performance across the full range of observation angles. Regardless of changes in viewing geometry, it consistently preserves image quality, suggesting that  $P_s$  is less sensitive to angle-induced scattering effects. Nevertheless, its ability to highlight material differences remains at a satisfactory level.

The  $DoP$  shows more promising results. With increasing observation angle,  $DoP$  exhibits a marked enhancement in imaging quality. Although its material discrimination capability slightly decreases at very high angles, it generally remains robust, making it a reliable indicator for distinguishing targets with different depolarization behaviors. Furthermore, observables such as  $P_\Delta$ ,  $P_2$ ,  $P_3$ ,  $DET$  and  $TRA$  demonstrate non-monotonic angular dependence: their imaging performance initially improves with angle, reaching a peak, and subsequently declines beyond a certain threshold. In most cases, the best discrimination performance is observed around an observation angle of  $70^\circ$ .

In summary, these results highlight the potential of polarimetric observables for distinguishing objects with different polarization characteristics. However, whether these observables outperform traditional intensity-based imaging in mitigating scattering-induced interference still requires further verification through simulation. Moreover, the results indicate that different observables exhibit varying sensitivities to different target materials, underscoring the importance of observable selection in polarization-based imaging systems.

### 3.2. Differences in imaging effects under different incident light observation angles in clear atmospheric environments

To further investigate the polarization characteristics inherent in spontaneous emission, this study systematically evaluates the imaging performance of various polarimetric observables under different observation angles in the presence of a complex scattering medium. Although the observation angles are carefully selected to ensure relatively optimal overall imaging quality, the experimental results indicate that both the intensity  $I$  and the observable  $P_1$  still exhibit suboptimal performance. Specifically, as shown in Fig. 4, these two observables fail to clearly present target details and provide very limited target-relevant features, making them inadequate for meeting the accuracy and validity requirements of subsequent analysis. The relatively poor performance of  $I$  can be attributed to its lack of resistance to scattering, which makes it highly susceptible to scattering-induced noise and background interference, thereby masking material-dependent differences. Similarly,  $P_1$  is strongly influenced by random fluctuations in polarization state and shows high sensitivity to observation angle, resulting in unstable image contrast and inconsistent feature delineation. Compared with other polarization observables—such as  $DoP$ ,  $TRA$ , or  $DET$ —that are more robust to scattering effects and better capture material-specific polarization signatures,  $I$  and  $P_1$  fail to provide reliable or interpretable information. Consequently,  $I$  and  $P_1$  are excluded from further in-depth investigation in this study.

Fig. 5 presents the imaging results of the remaining polarimetric observables across multiple observation angles. Each column corresponds to a specific observation angle, facilitating direct visual comparison of how each observable responds to changes in viewing geometry. This analysis enables a more comprehensive understanding of the angular dependence of polarimetric imaging performance in scattering-dominated environments, and provides valuable insights for observable selection in practical remote sensing applications.

A comprehensive analysis of the imaging results for  $DoP$ ,  $P_\Delta$ ,  $P_2$ ,  $P_3$ ,  $P_s$ ,  $P_p$ ,  $DET$ , and  $TRA$  under observation angles of  $30^\circ$ ,  $40^\circ$ ,  $50^\circ$ ,  $60^\circ$ ,  $70^\circ$ , and  $80^\circ$  reveals distinct response characteristics among different polarimetric observables when applied to target imaging. Notably,  $DoP$  exhibits a significant improvement in imaging performance within the  $30^\circ$ – $70^\circ$  observation angle range, as also demonstrated in Fig. 3. The imaging contrast and boundary clarity consistently improve with increasing angle in this range. However, beyond  $70^\circ$ , the influence of the scattering environment becomes more pronounced, overshadowing the benefits gained from increased observation angle. This unique angular response behavior, along with regional variations in imaging quality, effectively highlights the interplay between observation angle and scattering environment in determining imaging performance.

In comparison, although the overall imaging performance of  $P_\Delta$ ,  $P_2$  and  $P_3$  is inferior to that of  $DoP$ , these observables are still capable of delineating part of target contours within the  $40^\circ$ – $80^\circ$  range. Referring

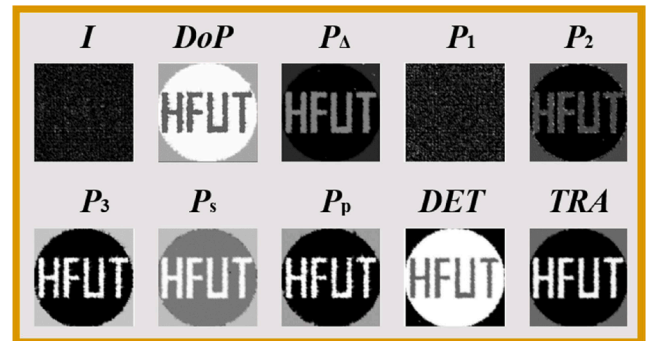


Fig. 4. The polarimetric observables in a clear-sky environment at an observation angle of  $70^\circ$ .

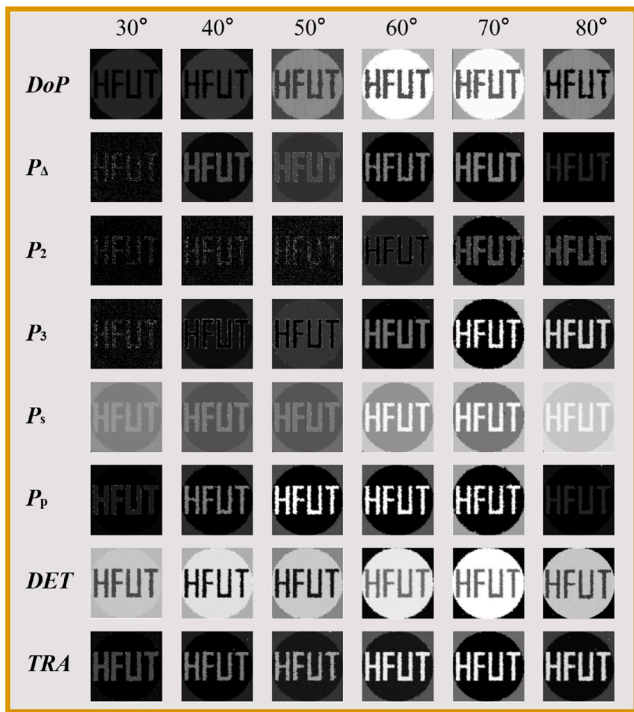


Fig. 5. The polarimetric observables at different angles in a clear-sky environment.

to Fig. 3, it is evident that scattering effects significantly influence their imaging outcomes. As the observation angle increases, these observables demonstrate an initial enhancement in resistance to scattering interference, followed by a decline beyond a certain threshold. This non-monotonic trend suggests that their effectiveness is closely tied to both angular geometry and the complexity of the scattering environment.

The observable  $P_s$  shows a gradual variation in image brightness and uniformity with changing observation angle. It achieves relatively high imaging performance within the  $30^\circ$ – $60^\circ$  range but experiences notable degradation beyond  $70^\circ$ , similar to the behavior observed for  $P_\Delta$ ,  $P_2$  and  $P_3$ . In contrast,  $P_p$  demonstrates enhanced contrast and more distinct target edges within the  $50^\circ$ – $70^\circ$  range, suggesting its potential advantage for target feature enhancement under specific angular conditions.

The  $DET$  exhibits characteristic bright spots at observation angles of  $60^\circ$  and  $70^\circ$ , indicating complex interactions with the scattering environment. This suggests its potential value in identifying intricate polarization scattering patterns. Meanwhile,  $TRA$  maintains relatively stable imaging performance across all observation angles, with minimal target deformation. As further evidenced by the imaging results presented in Figs. 3 and 5,  $DET$  exhibits superior stability against variations in observation angle compared to other polarimetric observables. This indicates that  $DET$  is less susceptible to angle-induced degradation caused by scattering effects, thereby offering a significant advantage for consistent target detection and recognition across varying observation angles conditions. In contrast,  $TRA$  shares a similar angular trend with  $DoP$ —both display a rise followed by a decline in imaging performance as the angle increases. However,  $TRA$ 's response curve is noticeably smoother, suggesting a more gradual transition and better overall stability.

To further support the above conclusions, the imaging data are normalized and plotted with the observation angle as the horizontal axis to enable a more intuitive comparison of the polarimetric characteristics of three target materials—copper, plastic, and stone. Smooth curves are used to connect the data points, as illustrated in Fig. 6. A representative set of polarimetric observables, namely  $DoP$ ,  $P_p$  and  $TRA$ , is selected for

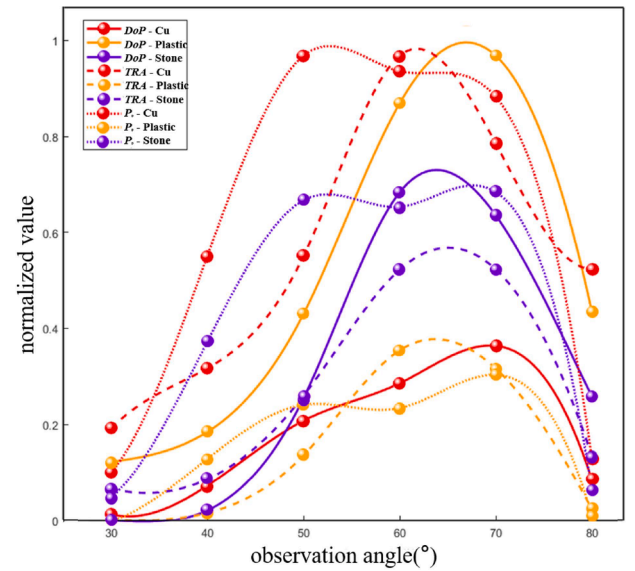


Fig. 6. Imaging responses of  $DoP$ ,  $P_p$ , and  $TRA$  of the target under different observation angles.

visualization. In the plot, three colored curves (red, orange, and purple) correspond to different regions of the target. The results clearly reveal a consistent trend: all three observables exhibit a rise-and-fall behavior with increasing observation angle, reaching their respective peaks within the  $50^\circ$ – $80^\circ$  range. More specifically, the  $DoP$  curves for all three materials show a steady increase with angle, peaking around  $60^\circ$ – $70^\circ$ . Among them, copper consistently exhibits the lowest  $DoP$  values, followed by stone, while plastic shows the highest. This can be attributed to differences in surface roughness among the selected materials—copper having the roughest surface and plastic the smoothest. A similar trend is observed for  $TRA$ , with all three materials reaching a maximum around  $60^\circ$ – $70^\circ$ , and copper maintaining relatively high  $TRA$  values across the entire angular range. In contrast, the  $P_p$  values show a more moderate variation between  $50^\circ$  and  $70^\circ$ , yet copper still consistently exhibits the highest  $P_p$  values at all angles.

These variations in peak positions and inter-material differences highlight the strong material discrimination capability of these polarimetric observables. They effectively capture the angular scattering characteristics of different surface types, thereby enhancing the potential for target classification and identification in complex environments.

Overall, most polarimetric observables demonstrate effective target contour delineation and satisfactory imaging quality within the low-to-mid observation angle range ( $30^\circ$ – $60^\circ$ ). As the observation angle increases,  $DoP$ ,  $P_\Delta$ ,  $P_2$ ,  $P_3$ , and  $P_p$  exhibit enhanced performance, with  $DoP$  achieving the highest material differentiation around  $70^\circ$ . However, beyond this threshold ( $70^\circ$ – $80^\circ$ ), a noticeable decline in performance is observed for several observables—such as  $DoP$  and  $TRA$ —due to the dominant influence of scattering effects, which begin to outweigh the benefits of larger angles. This angular dependence underscores the importance of selecting observables with stable performance across varied conditions. In particular,  $DET$  exhibit strong robustness against scattering-induced degradation, maintaining stable imaging performance across all tested angles. Collectively, these results affirm the potential of polarimetric observables for improving target detection and recognition in complex scattering environments.

#### 4. Conclusion

This study presents a comprehensive remote sensing framework that integrates infrared spontaneous emission modeling with a layered polarimetric radiative transfer model, aiming to analyze and enhance

imaging performance in scattering-dominated environments. Based on realistic atmospheric conditions, the system simulates the spontaneous emission behavior of targets and reconstructs the MM to extract ten commonly used polarimetric observables. These observables are then systematically evaluated under multiple observation angles to assess their angular sensitivity as well as their effectiveness in target detection and recognition.

The results demonstrate the strong potential of polarimetric observables for target detection and recognition in complex scattering environments. While intensity  $I$  and the observable  $P_1$  fail to effectively distinguish targets under such conditions, other observables—such as  $DoP$ ,  $P_\Delta$ ,  $P_2$ ,  $P_3$ ,  $P_p$ ,  $DET$ , and  $TRA$ —exhibit notable advantages in analysing polarization information relevant to target structure and material properties. Among them,  $DoP$  achieves the highest imaging clearest boundary delineation at an observation angle of approximately  $70^\circ$ , revealing its superior angular response. Observables  $P_s$  and  $P_p$  maintain relatively stable and detailed imaging performance within the  $30^\circ$ – $60^\circ$  range, underscoring their robustness under moderate angular conditions. Moreover,  $P_p$  is less sensitive to angular variations within the  $50^\circ$ – $70^\circ$  range, further confirming its stability across practical observation scenarios. Meanwhile,  $DET$  maintain consistent imaging effect across the full angular range and demonstrating potential for detecting complex polarization scattering phenomena. These findings collectively highlight the importance of observable selection in polarization-based imaging systems and validate the effectiveness of polarization observables in enhancing target detectability under atmospheric interference.

Overall, the study confirms the effectiveness of polarimetric observables derived from infrared spontaneous emission in achieving target detection under complex scattering conditions. Furthermore, it reveals the coupling mechanism between polarization characteristics, observation angle, and the scattering medium. Future work will focus on extending the model to dynamic environmental conditions, improving computational efficiency, and conducting cross-validation with experimental measurements and field data.

## Funding

This research was funded by the National Natural Science Foundation of China under Grant No. 61775050. The computational resources were provided by the HPC Platform of Hefei University of Technology.

## Data availability

Some or all data, models, or code that support the findings of this study are available from the corresponding author upon reasonable request.

## CRedit authorship contribution statement

**Haojie Ding:** Writing – original draft, Visualization, Validation, Software, Resources, Methodology, Investigation, Formal analysis, Conceptualization. **Xiaopeng Gao:** Visualization, Methodology, Investigation, Formal analysis, Data curation. **Xueqiang Fan:** Methodology, Investigation, Formal analysis, Data curation. **Zhongyi Guo:** Writing – review & editing, Supervision, Project administration, Methodology, Investigation, Funding acquisition, Formal analysis, Conceptualization.

## Declaration of competing interest

The authors declare that they have no competing financial interests or personal relationships that could have influenced the work reported in this paper.

## Data availability

Data will be made available on request.

## References

- [1] Schwanninger M, Rodrigues JC, Fackler K. A Review of Band Assignments in near Infrared Spectra of Wood and Wood Components. *J Near Infrared Spectrosc* 2011; 19(5):287–308.
- [2] Wang L, Yang Y, Tang X, et al. Combined multi-band infrared camouflage and thermal management via a simple multilayer structure design. *Opt Lett* 2021;46(20):5224–7.
- [3] Zheng S, Li H, Yu K, et al. Flexible multilayer film structure for visible–laser–infrared compatible camouflage. *Opt Lett* 2025;50(8):2747–50.
- [4] Huang L, Zhang W, Wei Y, et al. Flexible Ge/Cu/ZnSe multilayer photonic structures for triple-band infrared camouflage, visible camouflage, and radiative cooling. *Opt Express* 2024;32(21):37295–309.
- [5] Fan X, Lin B, Guo Z. Infrared Polarization-Empowered Full-Time Road Detection via Lightweight Multi-Pathway Collaborative 2D/3D Convolutional Networks. *IEEE Transactions on Intelligent Transportation Systems* 2024;25(9):12762–75.
- [6] Hu T, Shen F, Wang K, et al. Broad-Band Transmission Characteristics of Polarizations in Foggy Environments. *Atmosphere (Basel)* 2019;10.
- [7] Sano I, Mukai S, Okada Y. Aerosols all over the ocean and land, IGARSS 2001. Scanning the Present and Resolving the Future. In: *Proceedings. IEEE 2001 International Geoscience and Remote Sensing Symposium (Cat. No.01CH37217)*. 7; 2001. p. 3102–4.
- [8] Wang Y, Shang H, Letu H, et al. Impact of Orbital Characteristics and Viewing Geometry on the Retrieval of Cloud Properties From Multiangle Polarimetric Measurements. *IEEE Transactions on Geoscience and Remote Sensing* 2023;61: 1–17.
- [9] Popov A, Bortsova M. Detection of Metal Objects Against Mountain Ranges Using Polarization Transfer Functions. In: *2018 IEEE 17th International Conference on Mathematical Methods in Electromagnetic Theory (MMET)*; 2018. p. 290–3.
- [10] Li D, Xu C, Zhang M, et al. Measuring glucose concentration in a solution based on the indices of polarimetric purity. *Biomed Opt Express* 2021;12(4):2447–59.
- [11] Guo Z, Wang X, Li D, et al. Advances on theory and application of polarization information propagation(Invited). *Infrared Laser Engineering* 2020;49(6): 20201013.
- [12] Li L, Li Z, Huang Y, et al. Simulation of the polarization pattern of skylight affected by mineral dust aerosol particles. In: *2016 IEEE International Geoscience and Remote Sensing Symposium (IGARSS)*; 2016. p. 4093–5.
- [13] Shen F, Wang K, Tao Q, et al. Polarization imaging performances based on different retrieving Mueller matrixes. *Optik - International Journal for Light and Electron Optics* 2018;153:50–7.
- [14] Li D, Guo K, Sun Y, et al. Depolarization Characteristics of Different Reflective Interfaces Indicated by Indices of Polarimetric Purity (IPPs). *Sensors* 2021;21.
- [15] Li B, Chen Z, Lu L, et al. Cascaded frameworks in underwater optical image restoration. *Information Fusion* 2025;117:102809.
- [16] Li X, Goudail F. Vortex retarder-based Stokes polarimeters: optimal data processing and autocalibration capability. *Opt Lett* 2024;49(7):1696–9.
- [17] Fan X, Chen W, Lin B, et al. Improved polarization scattering imaging using local-global context polarization feature learning framework. *Opt Lasers Eng* 2024;178: 108194.
- [18] Tao Q, Sun Y, Shen F, et al. Active imaging with the aids of polarization retrieve in turbid media system. *Opt Commun* 2016;359:405–10.
- [19] Raković MJ, Kattawar GW, Mehruboglu MB, et al. Light backscattering polarization patterns from turbid media: theory and experiment. *Appl Opt* 1999;38(15):3399–408.
- [20] Shen F, Zhang B, Guo K, et al. The Depolarization Performances of the Polarized Light in Different Scattering Media Systems. *IEEE Photonics J* 2018;10(2):1–12.
- [21] Wang P, Li D, Wang X, et al. Analyzing Polarization Transmission Characteristics in Foggy Environments Based on the Indices of Polarimetric Purity. *IEEE Access* 2020; 8:227703–9.
- [22] Li D, Xu C, Lin B, et al. Research progress of polarization purity index theory and application. *Infrared and Laser Engineering* 2022;51(3):20210373. -1-73-13.
- [23] Tao Q, Guo Z, Xu Q, et al. Retrieving the polarization information for satellite-to-ground light communication. *Journal of Optics* 2015;17(8):085701.
- [24] Lin B, Fan X, Peng P, et al. Dynamic polarization fusion network (DPFN) for imaging in different scattering systems. *Opt Express* 2023;32:511–25.
- [25] Fan X, Lin B, Guo K, et al. TSMPN-PSI: high-performance polarization scattering imaging based on three-stage multi-pipeline networks. *Optic Express* 2023;31(23): 38097–113.
- [26] Lin B, Fan XQ, Li DK, et al. Research progress of imaging through scattering media based on deep learning. *Chinese Journal of Quantum Electronics* 2022;39(6):880.
- [27] Yu W, Shah SAA, Li D, et al. Polarized computational ghost imaging in scattering system with half-cyclic sinusoidal patterns. *Optics & Laser Technology* 2024;169: 110024.
- [28] Li X, Huang Q. Target detection for infrared polarization image in the background of desert. In: *2017 IEEE 9th International Conference on Communication Software and Networks (ICCSN)*; 2017. p. 1147–51.
- [29] Jiao Y, Zhang H, Zhi L, et al. Near-infrared Deep Imaging of Biological Phantom by Polarization Parametric Imaging. In: *2020 International Conference on UK-China Emerging Technologies (UCET)*; 2020. p. 1–4.
- [30] Duan J, Zheng Y, Chen G, et al. A multi-scale infrared polarization image fusion method based on polarization-forming. *Infrared Phys Technol* 2025;146:105735.
- [31] Shi H, Liu Y, He C, et al. Analysis of infrared polarization properties of targets with rough surfaces. *Optics & Laser Technology* 2022;151:108069.
- [32] Li D., Ma D., Guo K., et al. Polarization characteristics motivating target detection in different polarization spaces. 2024.



- [33] Suzuki S, Ogasawara N. Infrared thermographic test for removing background reflection based on polarization theory. *NDT & E International* 2019;103:19–25.
- [34] Motahar T, Rahman R, Hossain R. A Simulation Study on Light Scattering Effect on Water-borne Bacteriophage Virus Using Mie Analysis. In: 2017 IEEE 17th International Conference on Bioinformatics and Bioengineering (BIBE); 2017. p. 255–9.
- [35] Zhu J, Wang K, Liu H, et al. Modified model of polarized bidirectional reflectance distribution function for metallic surfaces. *Optics & Laser Technology* 2018;99: 160–6.
- [36] Hess M, Priest R. Comparison of polarization bidirectional reflectance distribution function (BRDF) models. In: 1999 IEEE Aerospace Conference. Proceedings (Cat. No.99TH8403). 4; 1999. p. 95–102.
- [37] Kallel A, Gastellu-Etchegorry JP. 3-D vector radiative transfer for vegetation cover polarized BRDF modeling. In: 2016 2nd International Conference on Advanced Technologies for Signal and Image Processing (ATSIP); 2016. p. 499–504.
- [38] Gil JJ. Structure of polarimetric purity of a Mueller matrix and sources of depolarization. *Opt Commun* 2016;368:165–73.
- [39] Lu SY, Chipman RA. Interpretation of Mueller matrices based on polar decomposition. *Journal of the Optical Society of America A* 1996;13(5):1106–13.
- [40] Li D, Ma D, Guo K, et al. Polarization characteristics motivating target detection in different polarization spaces. *Optics & Laser Technology* 2024;171:110430.
- [41] Torrance KE, Sparrow EM. Theory for Off-Specular Reflection From Roughened Surfaces\*. *J Opt Soc Am* 1967;57(9):1105–14.
- [42] Anxiang W, Zhensen W. Parameter inversion of shadowing function in light scattering model. *Infrared and Laser Engineering* 2014;43(1):332–7.
- [43] Priest RG, Gerner TA. Polarimetric BRDF in the Microfacet Model: theory and Measurements. In: Proceedings of the Meeting of the Military Sensing Symposia Specialty Group on Passive Sensors; 2000.
- [44] Mie G. Beitrage zur Optik trueber Medien, speziell kolloidaler Metalloesungen. *Ann Phys* 1908;330:377.
- [45] Rybicki GB. Radiative transfer. *Journal of Astrophysics and Astronomy* 1996;17(3): 95–112.
- [46] Raković MJ, Kattawar GW, Mehrübeoğlu M, et al. Light backscattering polarization patterns from turbid media: theory and experiment. *Appl Opt* 1999;38(15): 3399–408.
- [47] Wu D, Zhou J, Liu D, et al. 12-year LIDAR Observations of Tropospheric Aerosol over Hefei (31.9°N, 117.2°E). China. *Journal of the Optical Society of Korea* 2011; 15(1):90–5.
- [48] Ma D, Li D, Ding H, et al. Polarization Sensing Underwater Target Penetrating Complex Droplet-Bubble Layer. *IEEE Sens J* 2024;1. -1.